Brightness and Contrast Corrections for Space-Time Stereocorrelation via Proper Generalized Decomposition

Xuyang Chang, Corentin Le Gourriérec, François Hild, Stéphane Roux

Brightness and Contrast Corrections for Space-Time Stereocorrelation via Proper Generalized Decomposition

Xuyang Chang[1,2*], Corentin Le Gourriérec[2,3], François Hild[2] and Stéphane Roux[2]

[1]University of Science and Technology in Beijing, 30, Xueyuan Road, Haidian District, Beijing, 100030, China.
[2]Université Paris-Saclay, CentraleSupélec, ENS Paris-Saclay, CNRS, LMPS – Laboratoire de Mécanique Paris-Saclay, 4 avenue des Sciences, 91190 Gif-sur-Yvette, France.
[3]Saint-Gobain Research Paris, 39 quai Lucien Lefranc, 93303 Aubervilliers, France.

*Corresponding author(s). E-mail(s): xuyang.chang@ustb.edu.cn;

Abstract

Stereocorrelation (SC) is a flexible, non-contact experimental tool for measuring 3D shape and surface kinematics in complex mechanical tests. The violation of gray level conservation raises the issue of convergence of SC (*e.g.,* when local specular reflections are observed). Brightness and contrast corrections (BCCs) then become necessary. Space-time separation allows modes of the displacement, brightness, and contrast fields to be computed on the fly. The paper introduces a framework for Brightness and Contrast Corrections in Proper Generalized Decomposition stereocorrelation (BCCs-PGD-SC). It is shown that BCCs-PGD-SC improves the faithfulness of measured displacement fields and makes the identification of cracks viable from residual fields. The computational cost to include BCCs in PGD stereocorrelation is shown to be minimal within a PGD framework.

Keywords: Proper Generalized Decomposition, Stereo Digital Image Correlation, Brightness and contrast corrections

1 Introduction

The increasing performance of high-speed optical cameras has spurred dynamic mechanical tests since it allows displacement data to be measured from entire fields of view [1]. In addition to the broad range of spatial resolutions (from several micrometers to a few meters), significant progress has been achieved in fast optical imaging, as illustrated by the 30,000 Hz acquisition frequency used for current studies of crack propagation in laminated glass under projectile impact [2].

Digital Image Correlation (DIC) [3, 4], and one of its 3D extensions, namely, Stereocorrelation (SC or 3D-DIC [5–7]) are accurate, non-contacting, and robust methods to measure full-field kinematic data from acquired images. SC aims to measure 3D surface deformations between two states (reference and deformed configurations) using two or more cameras [3, 6, 8]. Similar to 2D-DIC, as for all displacement field measurements, these data can be used to calibrate constitutive parameters (using *e.g.,* Finite-Element Model Updating (FEMU) [9] or Integrated SC [6]). When temporal series are used for dynamic tests, the extension of SC to 4D fields (*i.e.,* 3D space and time) allows higher temporal resolutions (*i.e.,* higher frame rates) to be processed and more accurate and trustworthy identification results may be obtained.

Several challenges limit a broader usage of SC to process high-speed imaging:

– The computational speed of standard SC is relatively slow, especially for global approaches. Performing SC over long image series may become extremely time-consuming.

– During long time intervals, the gray levels may drastically change due to local specular reflections, kinematic changes, and cracks. Abrupt changes in gray levels may compete with kinematic unknowns and affect the convergence and accuracy of kinematic measurements.

In the early development of SC, "local" approaches were used to measure the 3D shape and its corresponding deformation, where the result is described as clouds of 3D scattered points [5]. The so-called Zero-Mean Normalized Sum of Squared Differences criterion (ZNSSD) [10, 11] is a popular method to account for brightness and contrast corrections. Such a method is equivalent to having a uniform brightness and contrast correction over each zone of interest, and the resulting (affine) corrections of gray levels are not recorded nor exploited. However, because more degrees of freedom (displacement, brightness, and contrast) are allowed for analyzing the same amount of information (images), the conditioning of the problem may degrade, as well as the measurement uncertainty.

Although kinematic fields are defined at every physical point, the underlined spatial regularity legitimizes using fewer degrees of freedom to represent the deformation without betraying its accuracy. Inspired by this philosophy, a dense (*i.e.,* "global") formulation of SC was proposed, using either facets [8, 12–14] or free-form surfaces [6, 15, 16] to describe the specimen surface and its deformation. The benefits of adopting global SC formulations are

two-fold. First, with fewer unknowns, the SC Hessian matrix becomes much better conditioned, and the displacement uncertainty is lowered [17]. Second, it allows the measured kinematic field to be directly compared to computed ones with isogeometric or finite-element discretizations, thereby opening ways to validate numerical simulations seamlessly.

Recently, improvements in the global formulation of SC have addressed the challenges above:

– A Proper Generalized Decomposition stereocorrelation framework (PGD-SC) has been proposed to increase the accuracy of kinematic measurements as well as computation speed [7, 18] (See Ref. [19] for a general overview of PGD approaches.)

– Brightness and contrast corrections in global SC were first reported by Charbal et al. [20, 21]. Later, a global formulation with BCCs was introduced with a spatial regularization strategy to filter out high-frequency components in BC fields by penalizing the L2-norm of their gradients [22].

As a natural extension, it is appealing to include Brightness and Contrast (BC) fields within a PGD-SC framework as extra parameters to be identified. Both displacement and BC fields are decomposed on the basis of spatial and temporal modes. PGD-SC introduces a progressive enrichment of the spatial-temporal modes for kinematic and BC fields, where modes are progressively added until reaching the final convergence of the global space-time residual. Moreover, different spatio-temporal regularization strategies may be included while preserving general formalism.

The proof of concept presented in this paper is a PVB laminated glass under projectile impact [18]. The large stereo-angles, local specular reflections, large-amplitude deformations, and severe BC variations make this test case extremely challenging and discriminative. It is shown that with proper spatio-temporal regularization, PGD-SC with BCCs outperforms standard SC. The numerical implementation in an existing global SC code required little effort, which is an additional benefit of this new implementation.

The novelties of the current work is summarized as follows:

– A unified and generalized PGD-SC framework is proposed to determine any physical quantities (*i.e.,* kinematic, brightness, contrast) expressed in a variational formulation.

– The temporal modes of each physical quantity are computed from the gradient of the cost function instead of space-time residual. The accuracy and the computational speed of constructing temporal shape functions are improved thanks to the proper weighting of the sensitivity and drastically reduced dimensionality.

– The staggered approach allows for a separated construction of temporal bases for both displacement (U) and brightness-contrast (BC) fields. This special feature leads to an efficient handling of local temporal phenomena that occur only to one or several physical quantities (*e.g.,* specular reflections only captured by one camera). Last, different temporal regularizations can be tailored for each quantity.

The paper is organized as follows.

In Section 2, the general principles of global and instantaneous SC, as well as brightness-contrast corrections are recalled. In Section 3, the generalized Space-Time PGD Stereocorrelation is detailed to register any physical fields that can be cast in a variational form. Then, in Section 4, the experimental set-up of the impact test is presented. Section 5 discusses the results obtained with the new implementations.

2 Formulation of SC with Brightness and Contrast Corrections

In the following, the concept of intrinsic texture is first defined. Standard (*i.e.,* instantaneous) SC with BCCs is then recalled.Different spatiotemporal regularization strategies for displacement and BC fields are finally discussed.

2.1 Stereo Calibration

The calibration of the stereoscopic cameras is crucial to link the 3D coordinates of the specimen with its 2D projections onto the different camera image planes [3], which reads for the i-th camera.

$$s^i\{\mathbf{x}^i\} = [\mathbf{\Pi}^i]\{\mathbf{X}\} \tag{1}$$

where $\{\mathbf{X}\} = \{X, Y, Z, 1\}^\top$ gathers the homogeneous coordinates of any point on the surface of the specimen, $\{\mathbf{x}^i\} = \{x, y, 1\}^\top$ the homogeneous coordinates of its 2D projection onto the i-th retinal image plane, $[\mathbf{\Pi}^i]$ the projection matrix for the i-th camera, and s^i the corresponding scale factor.

2.1.1 Intrinsic texture

Let us first assume that the calibration of the stereoscopic camera system was successfully achieved [2, 18]. Therefore, the intrinsic texture (*i.e.,* all physical points inside the region of interest (ROI), which are decorated by speckle patterns) is accurately estimated by taking the average of normalized reference images (with a mean μ equal to 0 and a standard deviation σ of 1)

$$\widetilde{f}^i(\mathbf{x}^i(\mathbf{X}, [\mathbf{\Pi}^i]), t_0) = \frac{f^i(\mathbf{x}^i(\mathbf{X}, [\mathbf{\Pi}^i]), t_0) - \mu(f^i)}{\sigma(f^i)} \tag{2}$$

$$\widehat{f}(\mathbf{X}) = \frac{1}{N}\sum_{i=1}^{N} \widetilde{f}^i(\mathbf{x}^i(\mathbf{X}, [\mathbf{\Pi}^i]), t_0) \tag{3}$$

where N is the total number of cameras, $\widetilde{f}^i(\mathbf{x}^i(\mathbf{X}, [\mathbf{\Pi}^i]), t_0)$ the normalized reference image for the i-th camera acquired at time $t = t_0$, $\mathbf{X}$ the position vector on the 3D surface, and $\mathbf{x}^i$ the corresponding position vector in the i-th camera plane.

2.2 Instantaneous SC

The formulation of instantaneous SC with BCCs was introduced in Ref. [20]. Later, complete BCCs were proposed in Ref. [22], where an L2-norm penalty of their gradients was applied to filter out high-frequency fluctuations. The formulation of instantaneous SC is briefly recalled; interested readers may refer to Refs. [6, 21, 22] for further details.

The FE-based formulation consists in measuring three fields, namely, displacement $\mathbf{U}(\mathbf{X},t)$, brightness $b^i(\mathbf{x},t)$ and contrast $c^i(\mathbf{x},t)$ by minimizing the global residual for *all* N cameras at time t. The corrected normalized deformed image for the i-th camera, $\widetilde{f}^i_{\mathbf{U}}(\mathbf{x}^i,t)$, for any displacement field $\mathbf{U}$ reads

$$\widetilde{f}^i_{\mathbf{U}}(\mathbf{x}^i,t) = \frac{\widetilde{f}^i(\mathbf{x}^i(\mathbf{X}+\mathbf{U}(\mathbf{X},t),[\mathbf{\Pi}^i])) - b^i(\mathbf{x}^i,t)}{1+c^i(\mathbf{x}^i,t)} \tag{4}$$

The brightness and contrast fields for reference images are defined on each image plane. Yet, thanks to the established calibration (1), the mapping of brightness and contrast fields in $\mathbf{x}^i$ is transported to $\mathbf{X}$. For reasons of simplicity, they are defined as $b^{(i)}(\mathbf{X},t)$ and $c^i(\mathbf{X},t)$ in the remainder of this paper, and the same holds for $\widetilde{f}^i(\mathbf{X},t)$. Local gray level residuals for the i-th camera are defined as

$$\rho^i(\mathbf{x}^i(\mathbf{X}),t) = \widehat{f}(\mathbf{X}) - \frac{\widetilde{f}^i_U(\mathbf{X}),t) - b^i(\mathbf{X},t)}{1+c^i(\mathbf{X},t))} \tag{5}$$

The local residual fields highlight all differences that are not captured or represented by the measured displacement and BC fields (*e.g.,* convergence, discretization error, noise, detector artifact, blur [20], or the presence of cracks [2]).

Assuming the gray-level conservation between the intrinsic texture and corrected deformed images acquired by each camera, the kinematic field and BC fields are sought to minimize

$$\begin{aligned}\eta^2(\mathbf{U},b,c) &= \sum_{i=1}^{N} \left\|\rho^i(\mathbf{x}^i(\mathbf{X}),t)\right\|^2 \\ &= \sum_{i=1}^{N} \int_{\mathrm{ROI}} \left[\widehat{f}(\mathbf{X}) - \frac{\widetilde{f}^i_{\mathbf{U}}(\mathbf{X},t) - b^i(\mathbf{X},t)}{(1+c^i(\mathbf{X},t))}\right]^2 \mathrm{d}\mathbf{X}\end{aligned} \tag{6}$$

It is worth mentioning that thanks to the normalization of each image, the sensitivity field for displacement, brightness, and contrast are of similar dynamic range; otherwise, the determination of $\mathbf{U}$ and BC may be prone to ill-conditioning.

The displacement, brightness, and contrast fields generally obey a certain level of regularity in the spatial domain. These fields are described using finite-element discretizations

$$\left\{\begin{array}{l} \mathbf{U}(\mathbf{X},t) \equiv \sum_{j=1}^{N_s} (a_U)_j(t)\boldsymbol{\Phi}_j(\mathbf{X}) \\ b^i(\mathbf{X},t) \equiv \sum_{j=1}^{N_s} (a_b^i)_j(t)\Phi_j(\mathbf{X}) \\ c^i(\mathbf{X},t) \equiv \sum_{j=1}^{N_s} (a_c^i)_j(t)\Phi_j(\mathbf{X}) \end{array}\right. \tag{7}$$

where $\boldsymbol{\Phi}_j$ denotes the (vectorial) j-th spatial shape function, Φ_j the corresponding scalar shape function, $\{\boldsymbol{a_U}(t)\}$ the column vector collecting all sought nodal displacements at time t, $\{\boldsymbol{a}_b^i(t)\}$ and $\{\boldsymbol{a}_c^i(t)\}$ the column vectors gathering the nodal brightness and contrast corrections for the i-th camera at time t.

One may determine the displacement and BC fields in one shot. Still, for the sake of simplicity of numerical implementations, a staggered "U-BCC-U" approach is used herein, where the BCCs step is performed independently for each camera.

2.2.1 Kinematic measurements

A Gauss-Newton scheme is used to determine the nodal displacements at each time t. The incremental corrections $\{\delta\boldsymbol{a}_U(t)\}$ of the nodal displacement at each iteration read

$$[\mathbf{H}_{\mathrm{U}}]\{\delta\boldsymbol{a}_U(t)\} = \{\mathbf{h}_{\mathrm{U}}(t)\} \tag{8}$$

where the spatial stereocorrelation Hessian matrix $[\mathbf{H}_{\mathrm{U}}]$ is expressed as

$$(H_{\mathrm{U}})_{jk} = \sum_{i=1}^{N} \int_{\mathrm{ROI}} \left(\boldsymbol{\Phi}_j(\mathbf{X}) \cdot \boldsymbol{\nabla}\widehat{f^i}(\mathbf{X})\right)\left(\boldsymbol{\Phi}_k(\mathbf{X}) \cdot \boldsymbol{\nabla}\widehat{f^i}(\mathbf{X})\right)\, \mathrm{d}\mathbf{X} \tag{9}$$

and the second member $\{\mathbf{h}_{\mathrm{U}}\}$

$$(\mathbf{h}_{\mathrm{U}}(t))_j = \sum_{i=1}^{N} \int_{\mathrm{ROI}} \left(\boldsymbol{\Phi}_j(\mathbf{X}) \cdot \boldsymbol{\nabla}\widehat{f^i}(\mathbf{X})\right)\rho^i(\mathbf{X},t)\, \mathrm{d}\mathbf{X} \tag{10}$$

are assembled. The instantaneous displacement field at iteration it is updated with the corresponding correction $\delta\mathbf{U}^{(it)}(\mathbf{X},t)$

$$\mathbf{U}^{(it+1)}(\mathbf{X},t) = \mathbf{U}^{(it)}(\mathbf{X},t) + \delta\mathbf{U}^{(it)}(\mathbf{X},t) = \mathbf{U}^{(it)}(\mathbf{X},t) + (\delta\boldsymbol{a}_U(t))_j\boldsymbol{\Phi}_j(\mathbf{X}) \tag{11}$$

where Einstein's summation convention is used.

To estimate the registration quality, normalizing the gray level residual by the dynamic range $\mathrm{dyn}(\cdot)$ of the reference images is usually normalized to allow for a fair comparison across N cameras. A camera-wise residual field $\widetilde{\rho}^i(\mathbf{X},t)$

and a global instantaneous residual $\rho_{\text{inst}}(t)$ are defined as

$$\widetilde{\rho}^i(\mathbf{X},t) = \frac{\rho^i(\mathbf{X},t)}{\text{dyn}(\widehat{f^i})} \tag{12}$$

$$\rho^i_{\text{inst}}(t) = \sqrt{\langle \rho^i(\mathbf{X},t)\rangle^2_{\mathbf{X}}} \tag{13}$$

$$\varrho_{\text{inst}}(t) = \sqrt{\frac{1}{N}\sum_{i=1}^{N}(\rho^i_{\text{inst}}(t))^2} \tag{14}$$

where $\langle\cdot\rangle_{\mathbf{X}}$ denote spatial averages over the considered ROI.

2.2.2 Brightness and Contrast corrections (BCCs)

After reaching a pre-converged solution for the kinematic field, BCCs are performed between the intrinsic texture and the corrected deformed images to restore the desired gray level conservation. For the i-th camera, the instantaneous BCC Hessian matrix assumes the following expression

$$[\mathbf{H}^i_{\text{BCC}}] = \begin{bmatrix} \mathbf{H}^i_{\text{bb}} & \mathbf{H}^i_{\text{bc}} \\ (\mathbf{H}^i_{\text{bc}})^\top & \mathbf{H}^i_{\text{cc}} \end{bmatrix} \tag{15}$$

where the sub-Hessian matrices $[\mathbf{H}^i_{\alpha\beta}]$ are given by

$$\left(H^i_{\alpha\beta}\right)_{jk} = \int_{\text{ROI}} \left(\Phi_j(\mathbf{X})S^i_\alpha(\mathbf{X})\right)\left(\Phi_k(\mathbf{X})S^i_\beta(\mathbf{X})\right)\ \text{d}\mathbf{X}, \tag{16}$$

for any α or β standing for either brightness b or contrast c. $S^i_b(\mathbf{X})$ and $S^i_c(\mathbf{X})$ denote respectively the sensitivity fields for brightness, b, and contrast, c, fields for the i-th camera. The BC second member reads

$$\{\mathbf{h}^i_{\text{BCC}}(t)\} = \begin{Bmatrix} \mathbf{h}^i_{\text{b}}(t) \\ \mathbf{h}^i_{\text{c}}(t) \end{Bmatrix} \tag{17}$$

with

$$\left(h^i_\alpha(t)\right)_j = \int_{\text{ROI}} \left(\Phi_j(\mathbf{X})S^i_\alpha(\mathbf{X})\right)\rho^i(\mathbf{X},t)\ \text{d}\mathbf{X}, \tag{18}$$

The brightness and contrast corrections are estimated by solving the following linear system

$$[\mathbf{H}^i_{\text{BCC}}] \begin{Bmatrix} \boldsymbol{a}^i_b(t) \\ \boldsymbol{a}^i_c(t) \end{Bmatrix} = \left\{\mathbf{h}^i_{\text{BCC}}(t)\right\} \tag{19}$$

The displacement field is first updated in the "U-BCCs-U" scheme until the residual reaches a stationary value. Then, the BCCs (between the intrinsic

texture and corrected deformed images) and kinematic corrections are alternatively computed until reaching final convergence, which is estimated with the following criterion,

$$\left\| \frac{\delta \rho_{\text{inst}}^{(it)}}{\rho_{\text{ints}}^{(it)}} \right\| \leq 10^{-5} \tag{20}$$

The complete instantaneous SC algorithm with BCCs is summarized in Algorithm 1

Algorithm 1 Instantaneous SC with BCCs

```
Compute normalized reference images f̃^i and intrinsic pattern f̂   ▷ Eq. (3)
Compute SC Hessian matrix                                          ▷ Eq. (9)
Compute BCC Hessian matrix                                         ▷ Eq. (15)
while t ≤ t_f do
    while residual stationarity not reached do
        Update SC second member                                    ▷ Eq. (10)
        Compute displacement corrections                           ▷ Eq. (8)
        Update displacement field                                  ▷ Eq. (11)
        Update corrected deformed images                           ▷ Eq. (4)
        if pre-convergence reached then
            Update BCC right-hand member                           ▷ Eq. (17)
            Compute brightness and contrast fields for all f̃^i    ▷ Eq. (19)
            Update deformed images with BCCs                       ▷ Eq. (4)
        end if
    end while
    U(X, t+1) ← U(X, t)
    t ← t+1
end while
```

3 Brightness-Contrast Corrections for Space-Time Proper-Generalized-Decomposition Stereocorrelation (BCCs-PGD-SC)

In this section, space-time stereocorrelation to perform registrations is first recalled. Then, the space-time PGD approach to stereocorrelation is generalized to express any physical field (*e.g.,* U,B, C) within the same formalism. This generalization is a novel and original contribution of the present paper.

3.1 Space-time formulation

For kinematic registrations,the expected spatiotemporal regularity legitimizes the use of a much lower number of degrees of freedom in both space and time domains, using a spatiotemporal finite element formulation, namely, using

nodal values instead of all the integration points (up to several million points in space)

$$\mathbf{U}(\mathbf{X},t) \approx \sum_{j=1}^{N_s}\sum_{m}^{N_t}(\alpha_U)_{jm}\mathbf{\Phi}_j(\mathbf{X})\Psi_m(t) \tag{21}$$

where $\Psi_m(t)$ are temporal shape functions whose number is N_t, and $\{\boldsymbol{\alpha}_U\}$ gathers all space-time nodal displacements. Similar expressions are obtained for the brightness and contrast fields, and the corresponding unknowns are $\{\boldsymbol{\alpha}_b\}$ and $\{\boldsymbol{\alpha}_c\}$. They are obtained as a natural extension of instantaneous SC.

$$\begin{aligned}&\left(\{\boldsymbol{\alpha}_U^{sol}\},\{\boldsymbol{\alpha}_b^{sol}\},\{\boldsymbol{\alpha}_c^{sol}\}\right) = \\ &\underset{\{\boldsymbol{\alpha}_U\},\{\boldsymbol{\alpha}_b\},\{\boldsymbol{\alpha}_c\}}{\operatorname{argmin}} \sum_{i=1}^{i}\left\|\widehat{f}(\mathbf{X}) - \frac{\widetilde{f}_U^i(\mathbf{X},t) - b^i(\mathbf{X},t)}{(1+c^i(\mathbf{X},t))}\right\|^2_{\mathrm{ROI}\times[t_0,t_f]}\end{aligned} \tag{22}$$

As for the instantaneous version, the sought space-time displacement field $\mathbf{U}(\mathbf{X},t)$ is progressively updated using an iterative Gauss-Newton scheme.

$$\begin{aligned}&[\mathbf{M}_U]\{\delta\boldsymbol{\alpha}_U^{(it)}\} = \{\mathbf{m}_U\} \\ &\mathbf{U}^{(it+1)}(\mathbf{X},t) = \mathbf{U}^{(it)}(\mathbf{X},t) + (\delta\alpha_U)_{jm}^{(it)}\mathbf{\Phi}_j(\mathbf{X})\Psi_m(t)\end{aligned} \tag{23}$$

where the space-time Hessian matrix $[\mathbf{M}_U]$ and second member $\{\mathbf{m}_U\}$ are expressed as

$$\begin{aligned}(M_U)_{jkmn} &= (H_U)_{jm}(K)_{kn} \\ (m_U)_{jk} &= \int_{t_0}^{t_f}(h_U(t))_j\psi_m(t)\ \mathrm{d}t\end{aligned} \tag{24}$$

The "temporal" Hessian matrix $[\mathbf{K}]$ assumes the following expression

$$(K)_{jl} = \int_{t_0}^{t_f}\psi_j(t)\psi_l(t)dt \tag{25}$$

In a previous work [23], it was shown that if the temporal shape functions are orthonormal, then $[\mathbf{K}]$ is equal to the identity matrix. Thus, the space-time problem of SC consists of N_t independent linear systems using the instantaneous Hessian matrix.

3.2 Proper Generalized Decomposition formulation

In most cases, the temporal shape functions are unrestricted. Thus, either prior knowledge (*e.g.,* loading history or numerical simulation) or intuition is used for an "educated" guess. In most classical space-time approaches, the temporal shape functions are prescribed based on prior knowledge of the loading history.

Alternatively, one may update temporal modes on the fly based on registration residuals. The latter is often referred to as a "PGD" approach [7, 18, 23].

In the determination of any *physical* field $\mathbf{W}(\mathbf{X}, t)$ (be it displacement or BC) that is cast in a variational form, the same low-rank approximation can be sought. The temporal modes of $\mathbf{W}(\mathbf{X}, t)$ are computed from the corresponding right-hand member $m_W(\mathbf{X}, t)$ in the present global SC framework

$$\begin{aligned} m_W(\mathbf{X}, t) &= \sum_{i=1}^{N_t} e^i \widehat{\xi^i}(\mathbf{X}) \widehat{\Psi}^i(t) \\ &\approx \sum_{i=1}^{N_p} e^i \widehat{\xi^i}(\mathbf{X}) \widehat{\Psi}^i(t) \end{aligned} \tag{26}$$

where $\widehat{\xi^i}(\mathbf{X})$ and $\widehat{\Psi}^i(t)$ stand for respectively the i-th spatial and temporal modes, e^i denotes the corresponding eigenvalue. Spatial modes are still decomposed over a mesh

$$\widehat{\xi^i}(\mathbf{X}) = \sum_j \beta_j^i \Phi_j(\mathbf{X}) \tag{27}$$

Several comments are worth being made:

1. In previous work, the temporal modes were constructed by performing a Proper Orthogonal Decomposition (POD) over the space-time SC residuals [18]. The reasons to perform POD of the right-hand member were twofold:
   – First, constructing the temporal modes using the right-hand member allows for the reliable extraction of the more significant temporal modes (especially when the displacement amplitudes at given time frames are relatively small). In contrast with raw residuals, the right-hand member contains the sensitivity fields as weights. This weighting is naturally tailored to the use of residuals.
   – In addition, the POD truncation is much less costly when handling the right-hand member than the stereocorrelation residuals.
2. The best low-rank approximation of the right-hand member is used instead of taking all temporal modes exhaustively. The number of temporal modes N_p is chosen so that the "power" (*i.e.,* L2 norm) of the reconstruction error is less than a prescribed fraction ϵ

$$E_{\text{ac}}(N_p) \equiv \frac{\sum_{i=1}^{N_p} (e^i)^2}{\sum_{j=1}^{N_t} (e^j)^2} \geq 1 - \epsilon \tag{28}$$

In this way, several temporal modes are first computed. As they are orthonormal, they are chosen in the global space-time approach, thereby leading to as

many N_p independent SC problems (the memory load of each modal space-time problem is equivalent to an instantaneous run).

For any mode k, the PGD-SC problem to solve becomes

$$\begin{aligned}(\mathbf{H}_{\mathrm{W}})_{ij}\delta\boldsymbol{\alpha}_j^k &= \int_{t=t_0}^{t_f}(\sum_{l=1}^{N_p} e^l\beta_i^l\widehat{\Psi}^l(t))\widehat{\Psi}^k(t)dt \\ &= e^k\beta_i^k\end{aligned} \tag{29}$$

where $[\mathbf{H}_{\mathrm{W}}]$ stands for the spatial Hessian matrix for $W_i(t)$ (the index i refers to the i-th nodal degree of freedom) and $(\widehat{\boldsymbol{\xi}}^k(\mathbf{X}) = \sum_j \beta_j^k\Phi_j(\mathbf{X})$ and $\widehat{\boldsymbol{\psi}}^k(t))$ constitute its k-th PGD spatial and temporal modes.

In the same spirit as instantaneous SC, the space-time gray-level residual is normalized

$$\rho_{\mathrm{global}} = \frac{1}{t_f - t_0 + 1}\sum_{t=t_0}^{t_f}\rho_{\mathrm{inst}}(t) \tag{30}$$

The PGD-SC scheme is iterated until reaching final convergence

$$\left\|\frac{\delta\rho_{\mathrm{global}}^{(it)}}{\rho_{\mathrm{global}}^{(it)}}\right\| \leq 10^{-5} \tag{31}$$

3.3 "U-BCC-U" pathway

For the PGD scheme, all relevant fields (displacement and BC) may be determined altogether by properly weighing different sensitivity fields. However, since displacement and BC fields undergo different temporal histories (*e.g.,* local reflection captured by a given camera but not by the other one), having a unified temporal basis may limit the convergence speed and robustness. It is preferable to choose the 'U-BCC-U' pathway to determine $\mathbf{U}$ and BC sequentially, and the temporal modes $\widehat{\Psi}_{\mathrm{U}}(t)$ for $\mathbf{U}$ are directly obtained from the weighted kinematic right-hand member $h_U(t)$. In contrast, the temporal modes for BCCs $\widehat{\Psi}_{\mathrm{BCC}}(t)$ are constructed from the camera-wise BCC right-hand member $\{\mathbf{h}_{\mathrm{BCC}}(t)\}$.

After pre-convergence of $\mathbf{U}$ is reached,

$$\left\|\{\delta\boldsymbol{\alpha}_U^{(\mathrm{it})}\}\right\| \leq 1\ \mu\mathrm{m} \tag{32}$$

the BCC and $\mathbf{U}$ corrections are alternated until reaching final convergence. The complete algorithm of PGD-SC with BCCs is summarized in Algorithm 2

Algorithm 2 PGD-SC with BCC

```
Compute normalized reference images and intrinsic pattern        ▷ Eq. (3)
Compute instantaneous SC Hessian matrix                          ▷ Eq. (9)
Compute instantaneous BCC Hessian matrix                         ▷ Eq. (15)
while Residual stationarity not reached do
    Update space-time right-hand member for U                    ▷ Eq. (24)
    Update temporal modes from current right-hand member         ▷ Eq. (26)
    Update space-time displacement field                         ▷ Eq. (23)
    if Pre-convergence of U reached then
        Update space-time BCC right-hand member                  ▷ Eq. (24)
        Update temporal modes from BCC right-hand member         ▷ Eq. (26)
        Compute space-time BCC fields
        Update space-time BCC
    end if
end while
```

3.4 Regularization

For the studied test, spatial and temporal regularizations were already implemented and discussed (as recalled in Appendix A). Interested readers will find more details in Refs. [18, 22].

4 Experimental setup

The response of structures subjected to dynamic loadings is complex and often calls for sophisticated instrumentation. The motivation is a better characterization and, thus, more faithful modeling of their mechanical response to optimize their design concerning criteria such as maintaining structural integrity or ensuring people's safety. Laminated glass (*i.e.,* composite composed of two or more glass plies interleaved with polymeric interlayers, presently polyvinyl butyral or PVB) is used as glazing in many applications for its good optical properties (*e.g.,* color control, thermal insulation, UV reflection [24]) combined with an ability to resist against impact [25]. The latter is a mandatory criterion for manufacturers. Within the framework of EN 356 standard, large panes (0.9×1.1 m^2) of laminated glass should resist three successive impacts of a 4 kg steel ball, dropped from a height of 2 to 9 m [26], without being perforated. In-situ high-speed measurements of impact tests on laminated glass are very challenging due to many phenomena that may occur during a hard-body impact:

- After a very short initial elastodynamic deformation, the glass plies damage [27];
- Fragmentation becomes finer as the projectile propagates through the glazing [28];

- Then, the broken composite behaves like a membrane that deforms in a large strain regime. Delamination and stretching of the PVB layers are initiated, absorbing a large amount of the impact energy while preventing glass shards from flying away (*i.e.,* keeping them adherent to polymer layers [29–31]).

To monitor this type of test, a device concept has been first introduced [32], then built [28] to perform impacts on laminated glass in a repetitive and controlled way. The setup, which is known as *"cannon"*, reproduces a drop-ball test using the same impactor material and geometry on 300×300 mm^2 samples. A projectile is launched thanks to a compressed air device. It hits an indentor (initially at rest, a few centimeters away from the laminated glass plate) that strikes the center of the plate positioned in a circular window. The indentor made of steel is hemispherical with a radius of 50 mm. The device (Figure 1) has been further instrumented to measure the indentor position at high rates and its time-resolved kinetic energy during impact combined with two high-speed cameras ('1' and '2') to determine the 3D surface deformation of laminated glass deformation with an acquisition frequency of 30 kHz, via SC analyses [2]. Fast imaging required two powerful 400 W spotlights ('3') because of very short integration times (*e.g.,* ∼30 µs in the present case). The stereovision system was calibrated using a dihedron ('4') with a known pattern accurately drawn on its surface to perform quantitative kinematic analyses.

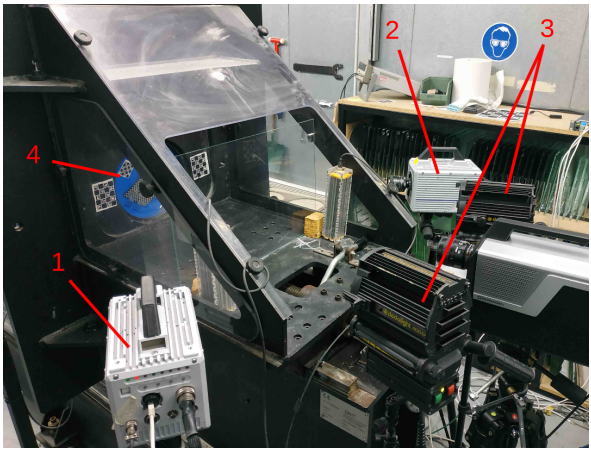

Fig. 1 Stereovision setup [18]. 1: Left-side camera. 2: Right-side camera. 3: 400 W dedolight® spots. 4: Observed sample or calibration target (presently, an "open-book") accurately positioned at the center of a 140 mm in radius window.

A speckle pattern (*i.e.,* black dots on a white background made of elastomer paints) was sprayed onto the observed rear side of the glazing (Figure 2). This choice was made to mitigate different very challenging aspects of the test for SC purposes, namely, glass fracture, large strain regimes, and brightness and contrast changes [2, 18, 22]. A portion of the surface was left transparent to

Table 1 DIC hardware parameters of the stereovision system [18]

Cameras	Photron® SA-5
Definition	640 × 376 pixels
Color filter	none
Gray Levels rendering	8 bits
Lens	Nikon AF Nikkor 24mm f/2.8D
Aperture	f/11
Field of view	500 mm × 300 mm = 0.15 m^2
Image scale	40 mm / 56 px≈ 0.7 mm/px (in the center)
Stereo-angle	right camera: 33°, left camera: 37°
Stand-off distance	between 70 and 80 cm
Image acquisition rate	30,000 fps
Patterning technique	B/W paints
Pattern feature size	3-10 pixels

track the crack formation and fragmentation, which are essential properties to evaluate the sample resistance against impact. The hardware parameters are listed in Table 1.

In Figure 2, the FE mesh used for SC measurements was projected onto both camera images. Its external radius was adjusted to avoid shadowing resulting from protruding edges, as seen by the camera. A very good consistency is observed, which validated the stereovision set-up calibration. In addition, leaving the center of the plate unpainted had two advantages:

- First, the contact of the impactor on the glass surface was accurately measured, allowing the duration between the elastic-dynamic deformation and the initiation of the first cracks in the glass plies to be captured.
- Second, the adjustment of the FE mesh, which shares the same boundary as the speckled region, was made more accurate.

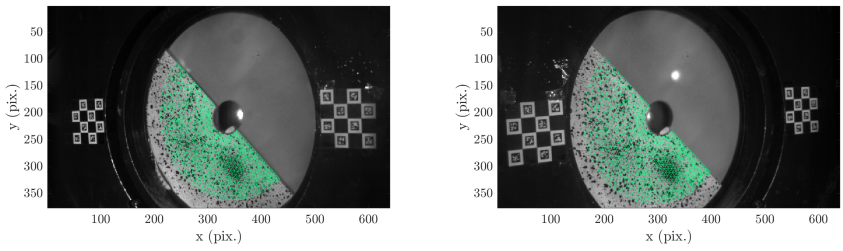

Fig. 2 Initial view from (a) left-side and (b) right-side cameras. The SC FE mesh (plotted in light green) is projected onto the speckled surface.

All the SC analysis parameters are gathered in Table 2. They are identical to those used in Ref. [18]).

Table 2 SC analysis parameters (identical to those reported in Ref. [18]).

DIC software	Correli 3.0 [33]
Image filtering	None
Element sizes	1.5-1.7 mm ($\approx 25-26$ px, see Figure 2)
Shape functions	Linear (T3 elements)
Evaluation points (per element)	528 (*i.e.,* $N_{\text{IP}} \approx 23$)
Matching criterion	Sum of squared differences (Equation (6))
Interpolant	Linear
Displacement noise-floor	$[\sigma(U_x), \sigma(U_y), \sigma(U_z)] = [8.2, 8.5, 4.7]$ µm

5 Results and discussions

In the following, qualitative observations of laminated glass under impact are made. The details of PGD implementations are then discussed. Last, the performance of PGD-SC and FE-based SC algorithms with and without BCCs are compared.

5.1 Qualitative observations

For the sake of simplicity, in the present work, the index t refers to the frame number in the image sequence, and the real-time t/F is easily obtained with the corresponding acquisition frequency $F = 30$ kHz. The interested reader is referred to previous publications [2, 18] for more details. The main points are briefly recalled hereafter. The initial impactor velocity was 7.53 m/s. By plotting stereo-image sequences at different instants of time (Figures 3 and 4), several qualitative observations are made:

1. Before $t = 50$, the projectile impactor has not yet reached the glass surface. The reference images are thus chosen as the stereo pair acquired when $t = 50$;
2. At $t = 70$ (*i.e.,* 0.67 ms after impact), radial cracks in glass have rapidly initiated and are first observed on the unspeckled region;
3. At $t = 90$ (1.33 ms after impact), orthoradial cracks have initiated and are seen along with the densification of radial cracks.
4. When $t \in [130, 150]$, specular lighting reflections occurred due to the glass surface large motion (and rotation). Specular reflections led to local brightness saturation (particularly for the first camera (Figure 3);
5. Between $t = 110$ and $t = 150$, a massive densification of orthoradial cracks took place;
6. Despite very large out-of-plane motions, the adhesion of glass with the laminated PVB layers successfully limited the detachment of small fragments. Some small pieces ejected from the sample center are observed at about $t = 250$ (*i.e.,* 6.6 ms after impact). The first fragment detachment occurred when $t = 247$. This phenomenon violates gray-level conservation, and the kinematics can no longer be faithfully captured;

7. After $t = 250$, the axisymmetry of the kinematic field is no longer valid due to the progressive localization of PVB tearing. The SC analysis was thus carried out when $t \in [50, 250]$ for these two reasons.

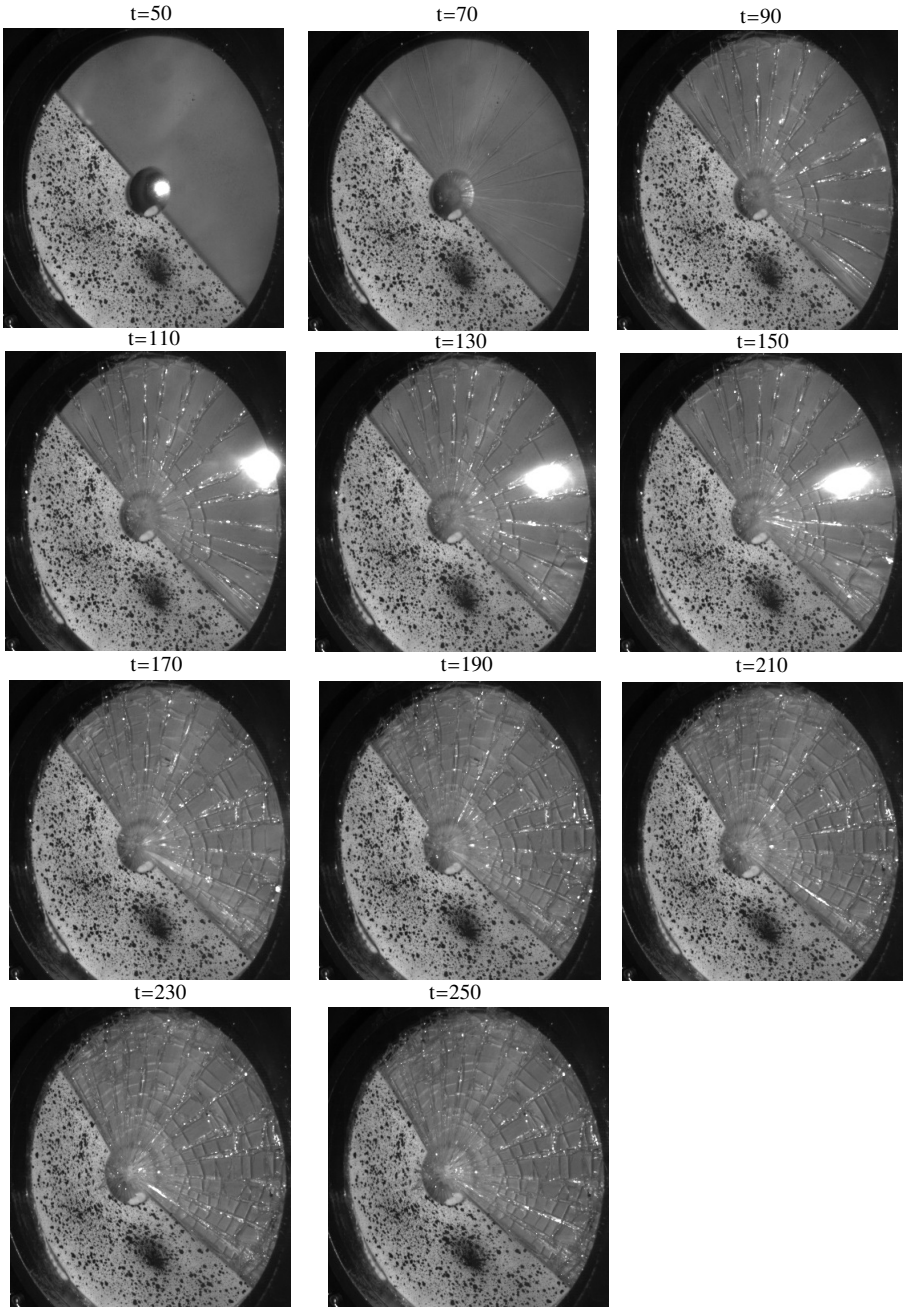

Fig. 3 Image sequence acquired by the first camera from $t = 50$ to 250, with a step size of 20

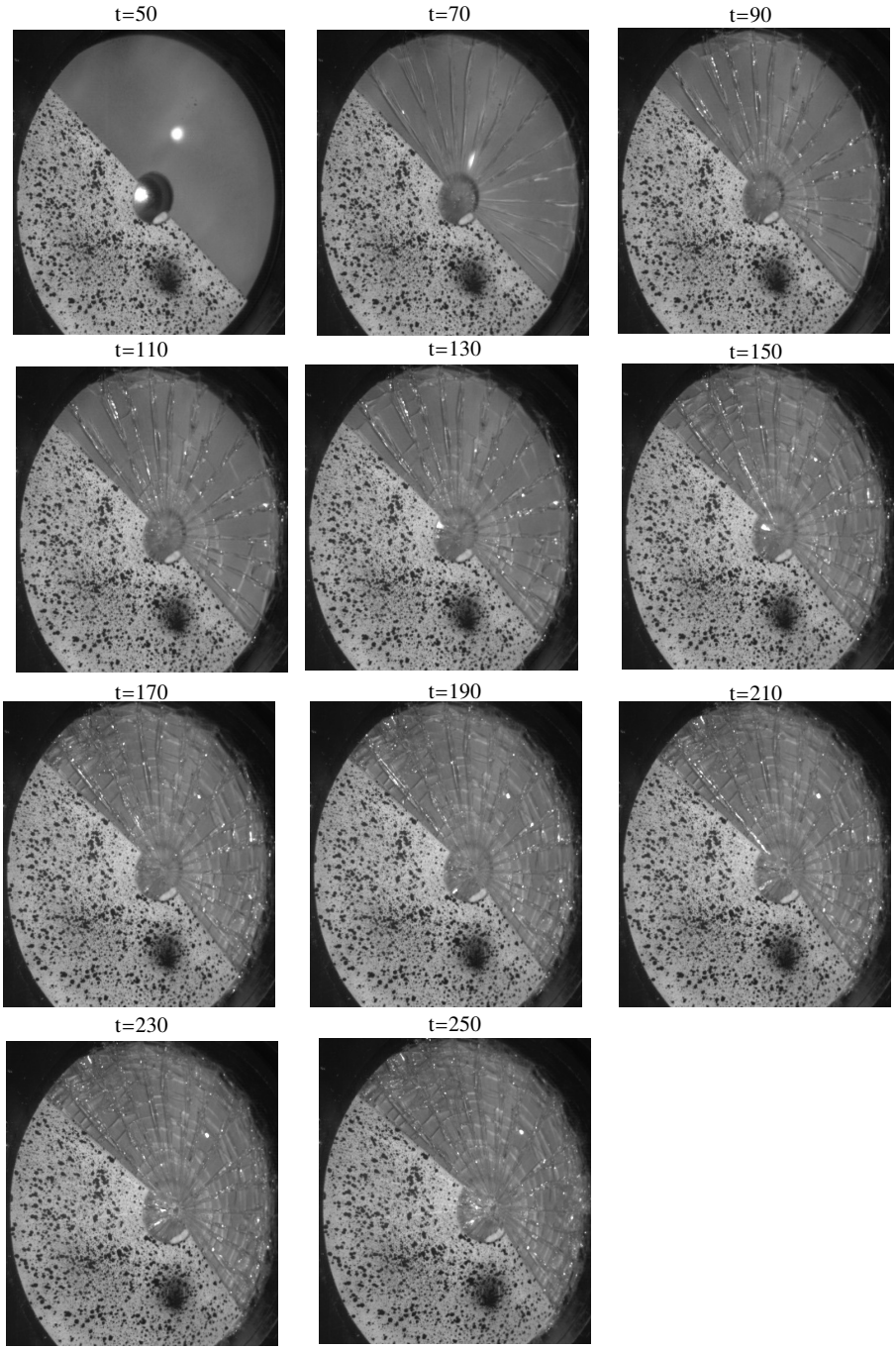

Fig. 4 Image sequence acquired by the second camera from $t = 50$ to 250, with a step size of 20

5.2 Temporal shape functions in PGD-SC

5.2.1 Temporal shape functions from the right-hand member.

The performance of the proposed PGD-SC algorithm using space-time residuals or space-time right-hand members to extract the temporal shape functions is first compared in Figure 5. When using space-time right-hand members, thanks to the drastically reduced dimensionality (*i.e.,* the space-time residual is a matrix with size 497280×250, while that of the right-hand member is only 1917×250), the POD extraction is much faster using space-time right-hand members.

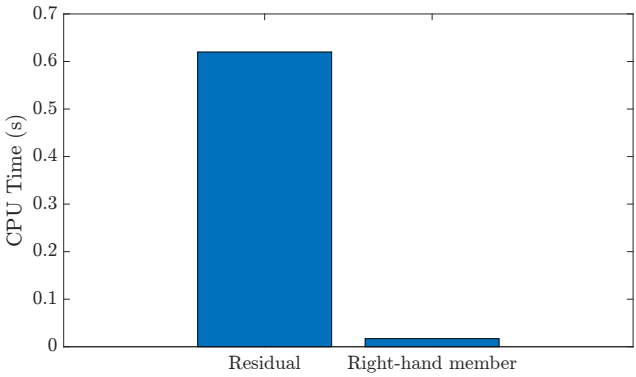

Fig. 5 Average CPU time for extracting POD modes from space-time residual and space-time right-hand member.

To evaluate the convergence and robustness of two PGD-SC variants, the dimensionless global residual is plotted against the iteration number in Figure 6. Due to the natural weighting of the sensitivity fields, the temporal shape functions constructed from the right-hand member are more accurate than those built from the residuals. As a result, the convergence and robustness of the new PGD-SC variant are slightly improved.

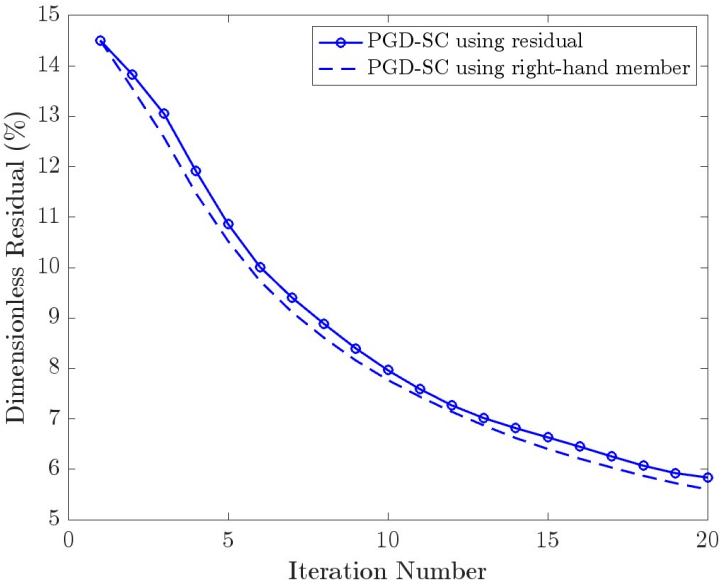

Fig. 6 Performance comparison of PGD-SC using two different methods to update temporal shape functions.

5.2.2 Separated construction of temporal shape functions for U and BC.

At pre-convergence of **U** in PGD-SC, (*i.e.,* the registration error is less than 5%), the relevant temporal modes of **U** and BC for each camera are plotted in Figure 7. Focusing on the temporal modes of BC fields for the first camera in particular (Figure 7(b)), its 2-nd and 3-rd temporal modes highlight the presence of local specular reflections ($t = 135$ and $t = 176$) and perturbations by glass fragments ($t = 247$). Let us stress that these spikes are not present in the temporal modes of the displacement, nor in the BC fields of the second camera (Figure 7)(a,c)). This result is consistent with the experimental observations reported in subsection 5.1. In this regard, the staggered approach, separating temporal mode reconstructions for **U** and BCCs in the proposed PGD-SC version, proves its efficiency in decoupling the kinematics from the effect of these local reflections.

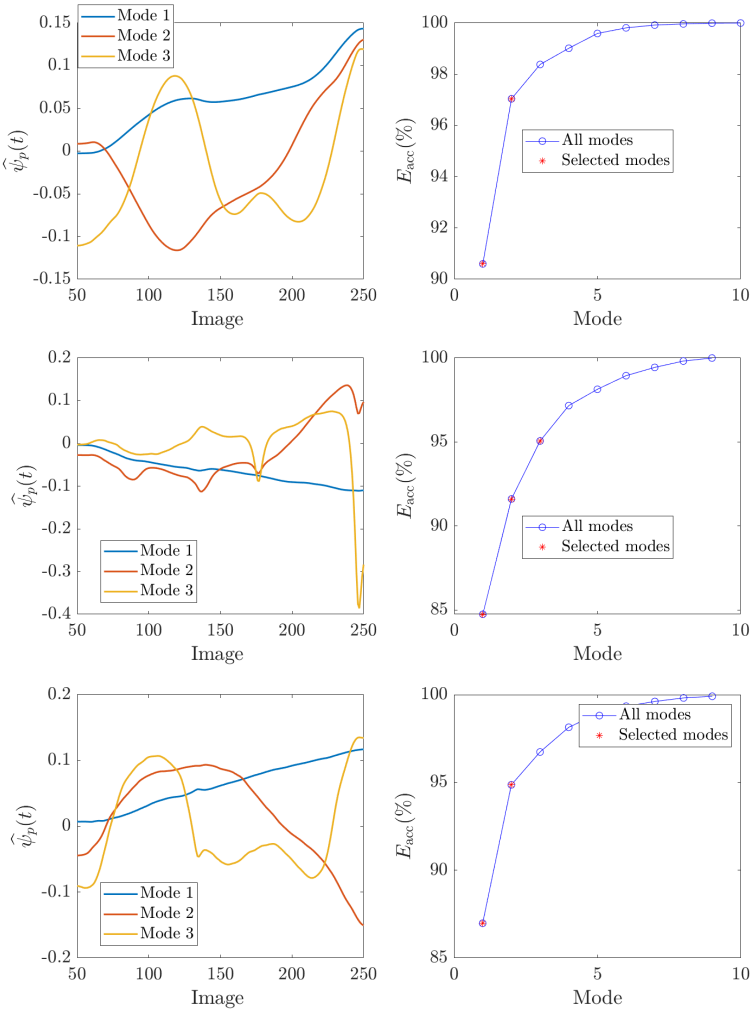

Fig. 7 Temporal modes constructed for (top) the kinematics, the BC field for cameras 1 (middle) and 2 (bottom)

5.3 Convergence

Figure 8 shows the convergence of PGD SC with BCCs. The global residual history is plotted in Figure 8(a). At iteration 25, the pre-convergence of U was reached, and BCCs and U corrections were alternated for each space-time iteration. The introduction of BCCs significantly decreased the global gray-level residual.

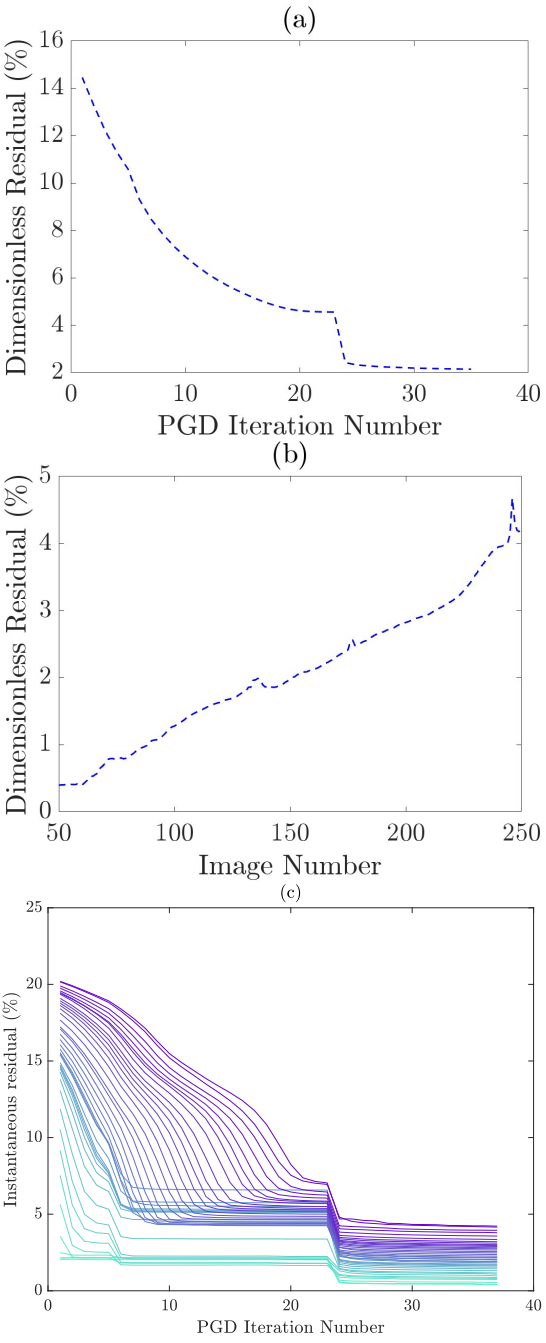

Fig. 8 Convergence of PGD-SC with BCCs. (a) Global residual vs. iteration number. (b) Converged instantaneous residual as a function of frame number. (c) Instantaneous residual history as a function of PGD iteration number. The global residual converged after 37 iterations. Before the 5-th iteration, the greedy approach was used (with one temporal mode), and afterward, more temporal modes were used to compute the space-time corrections. After 22 iterations, the pre-convergence of **U** was reached. BCCs and **U** are then alternated until final convergence (ca. 2.1%).

At convergence, Figure 8(b) shows the final global instantaneous residual as a function of frame number. The level varies from 0.5% to 4.5%. The spikes at $t = 135$ and $t = 176$ correspond to local specular reflections, while, at $t = 247$, it results from glass fragments flying into the region of interest for camera 1. The instantaneous residuals came back to 4.1% immediately after this event.

The instantaneous residual norm for each frame vs. iteration number is plotted in Figure 8(c) with a step size of 5. The local residuals from the first deformed image to the last are shown in shaded colors from light cyan to purple. The introduction of more temporal modes after the 5th iteration and the activation of BCCs after the 23rd iteration significantly improved the convergence of PGD-SC. It is worth noting that even though this test case is very challenging, the final global residual is very low (*i.e.,* just above 2%).

5.4 Temporal regularization of BC fields

To further study the influence of temporal regularization in BC fields, the same analysis is carried out with different regularization times for the temporal modes of BC fields, namely, $\tau_{BC} = [1, 2, 4, 8, 16, 32, 64]$ while the temporal regularization for $\mathbf{U}$ is set to $\tau_U = 10$. The global and local residuals are plotted in Figure 9. In the present case, if a very large regularization time is selected (*i.e.,* $\tau_{\mathrm{BC}} \geq 32$), the BCCs in the PGD-SC framework are unable to take into account local singular events (*i.e.,* specular reflections and local reflection from cracks that take place at $t = 135$ and 176, glass fragment flying into the region of interest $t = 247$). With a decreasing regularization time, such local events are better captured, leading to a gradual decrease in instantaneous residuals. However, if the applied temporal regularization becomes too small (*i.e.,* $\tau_{\mathrm{BC}} = 2$), the temporal Hessian matrix becomes ill-conditioned, and the local residual displays some oscillations (especially around $t = 247$). Hence, the best compromise is to adopt a moderate temporal regularization (*e.g.,* with $\tau_{BC} = 4$).

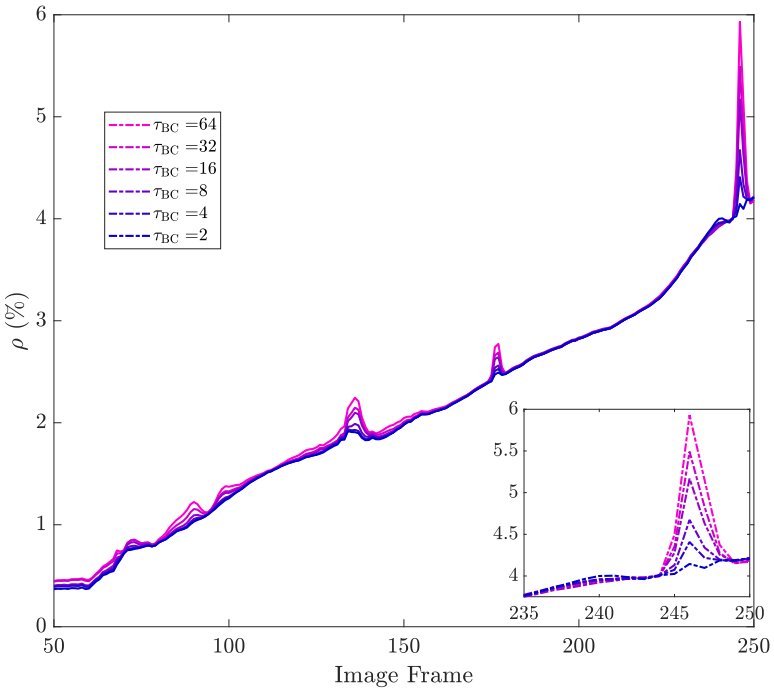

Fig. 9 Converged local residual using different temporal regularization for BCCs. Different curves are shown from the lowest (dark blue) to highest (light magenta) regularization times $\tau_{BC} = [2, 4, 8, 16, 32, 64]$.

5.5 Performance comparison

To fairly compare the performance between standard SC and PGD-SC enhanced with BCCs, the same FE mesh and convergence criterion are used:

- **Gray level residuals**. At projectile impact ($t = 50$), both approaches estimate the same instantaneous residual ($\rho = 0.25\%$). Their robustness is cross-validated. PGD-SC with BCCs has an overall lower residual than standard SC despite temporal regularization over $\mathbf{U}$ and BC fields. At the spikes where glass fragments ($t = 247$) took place, the instantaneous residual of PGD-SC is slightly higher than standard SC due to the enforced smoothness for temporal changes due to temporal regularization.

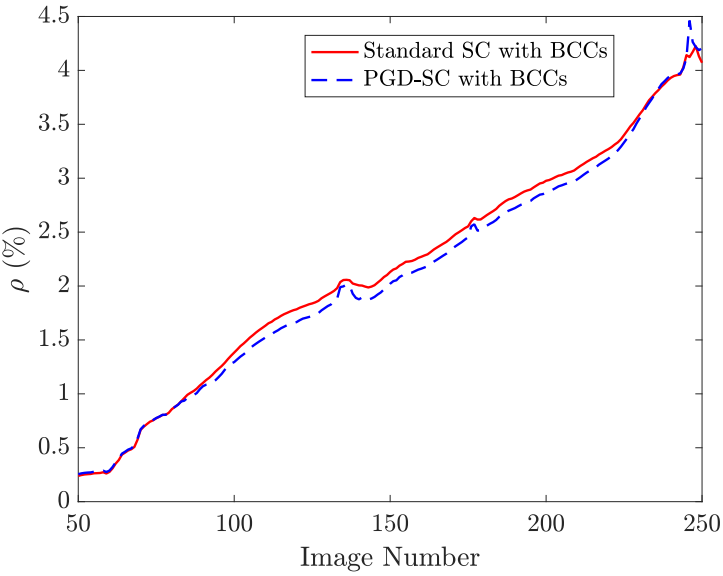

Fig. 10 Instantaneous residual history for standard SC with BCCs (red) and PGD-SC with BCCs (blue).

- **Displacement fields**. The nodal-wise radial and out-of-plane displacement components as functions of r are displayed with a step size of 10 in Figure 11. Thanks to the temporal regularization applied in PGD-SC (*i.e.*, $\tau_U = 10, \tau_{\text{BC}} = 4$), the high-frequencies component in $\mathbf{U}$ (especially for axial displacement components) for PGD-SC have been successfully filtered out.

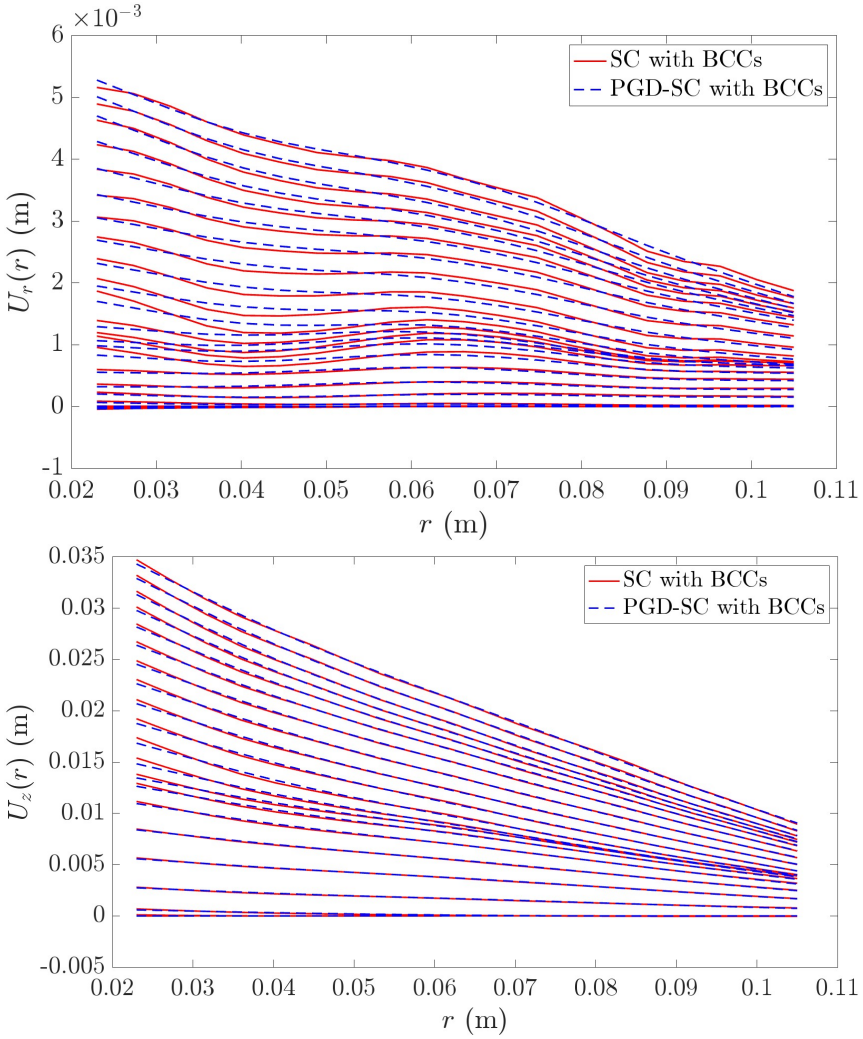

Fig. 11 Displacement field measured via PGD-SC and standard SC with BCC with a step size of 10 frames. Radial (a) and out-of-plane (b) displacements.

The camera-wise gray-level residual fields at frames 150, 180, and 240 are plotted in Figure 12 and Figure 13. At the late stages of impact, due to the large displacement amplitude, the gray-level conservation is not fulfilled between the reference image and displacement-corrected deformed images. Without BCCs, it is less straightforward to visualize the presence of cracks in the gray-level residuals. Conversely, by performing BCCs, the radial crack pattern is easily seen. Clearer observation of crack initiation is an additional benefit of the present technique, especially for numerical modeling purposes.

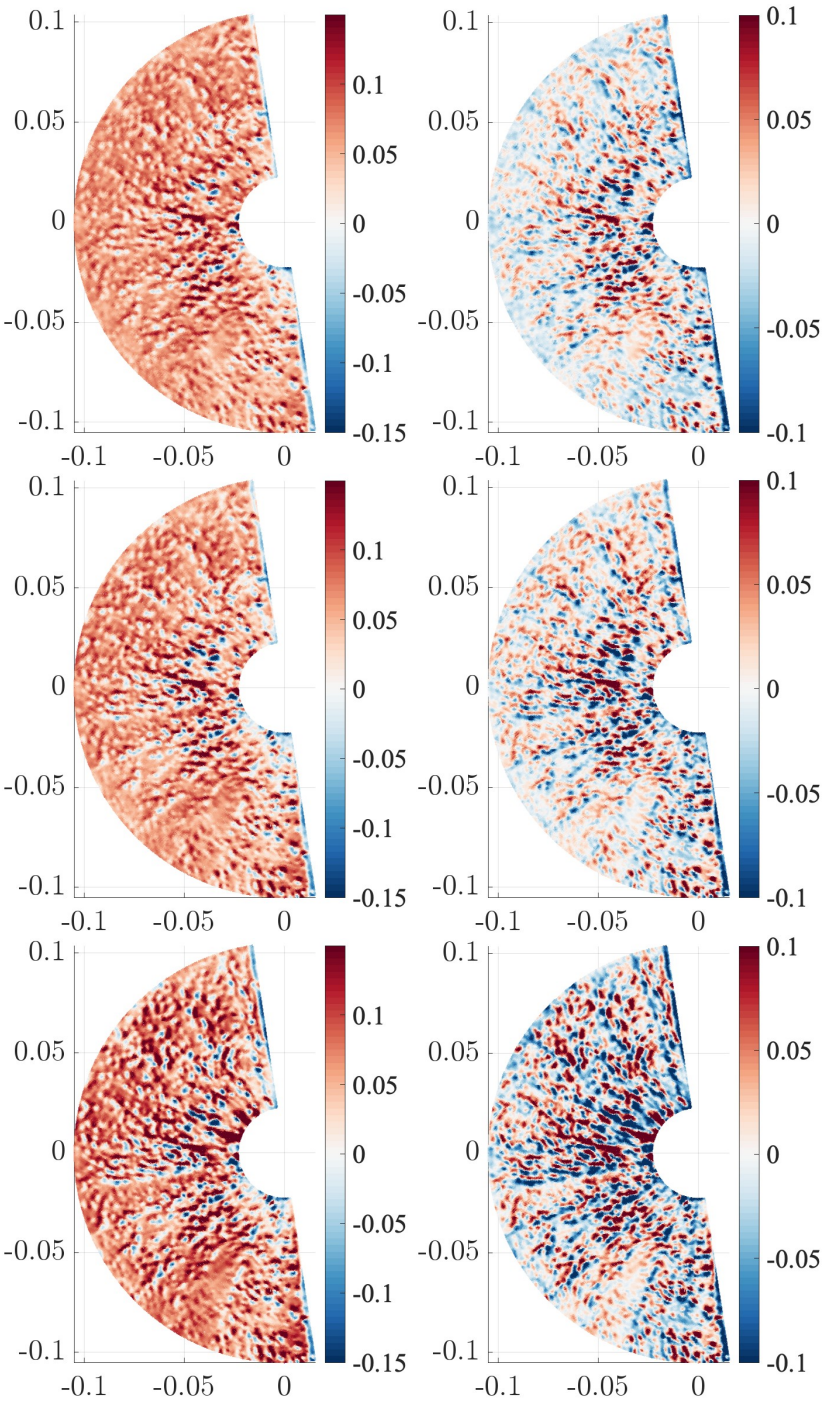

Fig. 12 Crack pattern observed on camera-wise gray-level residual fields for the first camera at frames 150, 180, 240. (left) With no BC correction, and (right) with BCCs

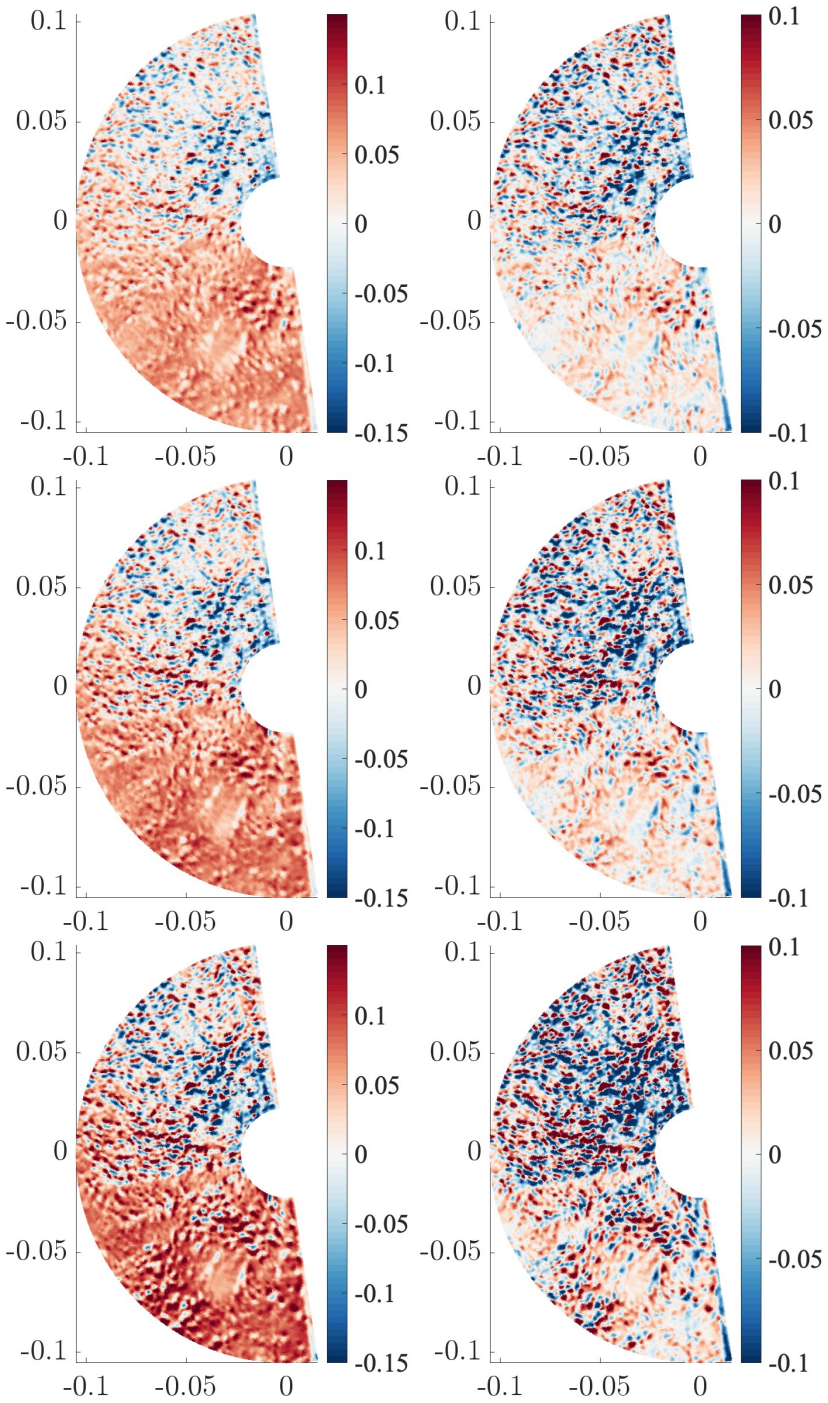

Fig. 13 Crack pattern observed on camera-wise gray-level residual fields for the second camera at frames 150, 180, 240. (left) With no BC correction, and (right) with BCCs

As an additional validation, the camera-wise gray-level residuals are back-projected onto each deformed image for frame 240. Through a direct comparison (Figure 14), one may correlate the observed crack patterns from the raw images with the gray-level residuals, qualitatively validating the robustness of the kinematic registrations.

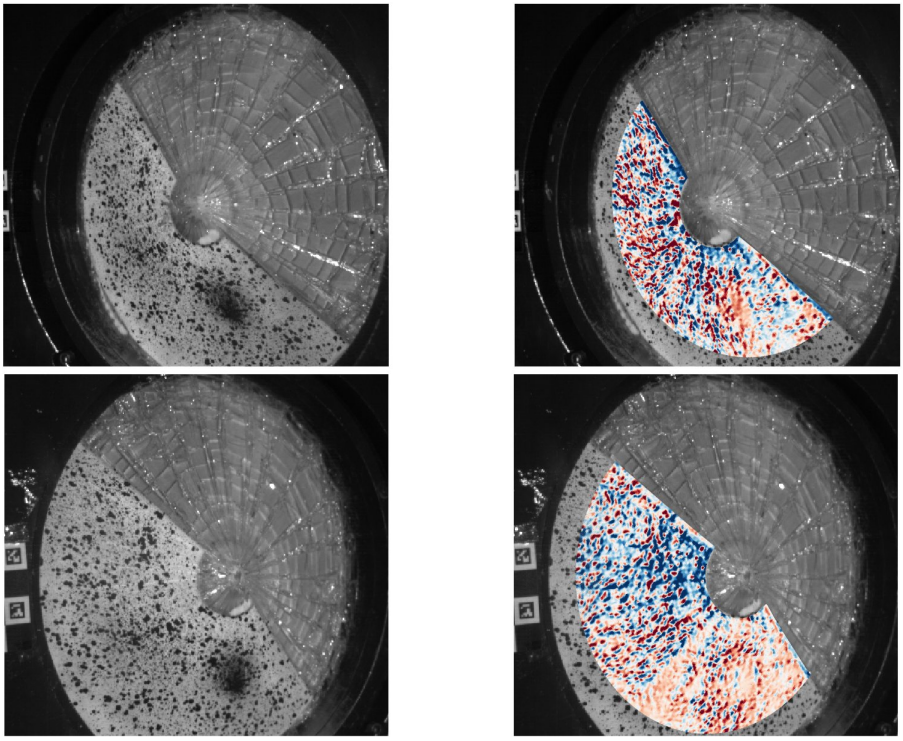

Fig. 14 Qualitative validation. (left) Deformed configurations for frame 240. (right) Gray-level residual re-projected onto each deformed image

For the performance comparison between standard SC and PGD SC, both enhanced with BCCs in Figure 15, PGD-SC converged slightly (13%) faster than standard SC despite an increased (5%) iteration number. The additional cost of computing the BC fields did not significantly slow down PGD-SC computations.

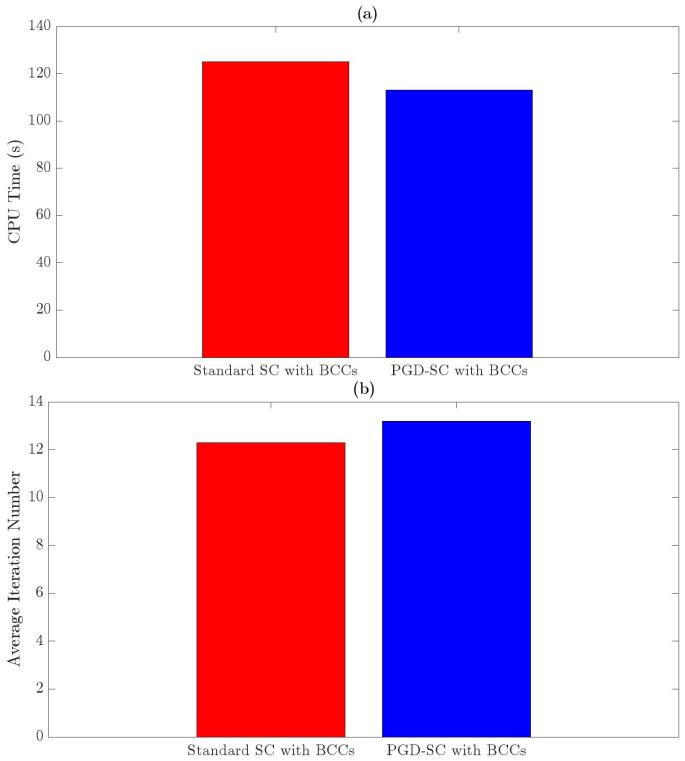

Fig. 15 Comparison in computational cost between standard SC and PGD-SC with BCCs. (a) Total CPU Time. (b) Average Iteration Number.

6 Conclusions

In the context of stereocorrelation (SC), the global formulation of SC enables easy access to PGD-SC. This approach exploits the intrinsic "simplicity" in time of the entire problem. Instead of using an exhaustive description, a few "modes" are sufficient to represent displacement and BC fields without betraying the tolerated accuracy.

A staggered "U-BCC-U" approach was used in the proposed PGD-SC framework since different spatiotemporal regularization strategies were needed to penalize displacement and BC fields. The staggered approach proved its versatility and flexibility in the present test case, where the displacement and BC fields did not vary similarly in space and time. The additional cost of computing BC fields did not significantly slow down the PGD-SC computations. Still, it resulted in a globally better kinematic description when compared to standard SC with BCCs.

During image registration, a few glass fragments detached from the tested sample and obscured a small zone for some frames after $t = 250$ as captured by the first camera (and remained out of the region of interest for the second

camera). This perturbation was a violation of gray-level conservation. The following registered images were disqualified from the SC analysis because of glass fragments and loss of gray-level conservation. In Ref. [34], a modal decomposition was carried out over an incomplete data set. Hence, performing PGD-SC with partial measurements (*i.e.,* when a few frames from one camera are missing) is an appealing perspective to the current PGD-SC framework.

A Spatial regularization for different physical quantities

A.1 Spatial regularization for kinematic fields

For the presented test case, the projectile hits the center of the clamped glass plate so that the kinematic field is considered axisymmetric (at least at the beginning of impact). Using the axisymmetry assumption, one can use much fewer spatial degrees of freedom to describe the kinematics of the tested sample since the displacement of each physical point (in polar coordinates) only depends on its initial radial distance to the impact center, r, instead of its full 2D coordinates of the surface in the global frame

$$\mathbf{U}(\mathbf{X},t) = U_r(r,t)\mathbf{e}_r + U_z(r,t)\mathbf{e}_z \tag{33}$$

However, the initial FE mesh does not conform to the axisymmetric formulation. A 1D radial discretization (mesh) is introduced in which the radial U_r and out-of-plane U_z displacements are expressed as functions of the radius r. This operation involves a rectangular transformation matrix $[\mathbf{T}]$ that relates each nodal displacement component to the axisymmetric discretization. Then, the axisymmetric reduction is obtained with a simple modification of the spatial Hessian matrix and right-hand member,

$$\begin{aligned} [\mathbf{H}_{(U,axis)}] &= [\mathbf{T}]^\top [\mathbf{H}_U][\mathbf{T}] \\ \{\mathbf{h}_{(U,axis)}(t)\} &= [\mathbf{T}]^\top \{\mathbf{h}_U(t)\} \end{aligned} \tag{34}$$

A.2 Spatial regularization for BCCs

As mentioned earlier, introducing BCCs leads to a significant increase in spatial degrees of freedom (from 3 to 5 per node), an increase in conditioning, and, consequently, uncertainties. One way to circumvent this issue is to introduce regularization and constrain the solution to live in a reduced subspace (*e.g.,* Tikhonov regularization [35]). However, in contrast with displacement, one cannot use axisymmetry to estimate BCCs because the orientation of the surface with respect to lighting sources changes during the test. Alternatively, adding a penalty on high spatial frequencies of BCCs is a way to limit the effective number of degrees of freedom.

Let us introduce $[\mathbf{D}_s^i]$ the discrete gradient operator integrated over all elements of the mesh so that the penalty term is proportional to

$$(\varphi_b^i)^2 = \{\boldsymbol{b}^i\}^\top [\mathbf{D}_s^i]^\top [\mathbf{D}_s^i]\{\boldsymbol{b}^i\} \tag{35}$$

$$(\varphi_c^i)^2 = \{\boldsymbol{c}^i\}^\top [\mathbf{D}_s^i]^\top [\mathbf{D}_s^i]\{\boldsymbol{c}^i\} \tag{36}$$

where one recognizes $[\mathbf{D}_s^i]^\top [\mathbf{D}_s^i]$ as the discrete Laplace operator.

The total cost function to minimize for BCCs of the i-th camera thus becomes

$$(\varphi^i)^2_{\text{total}} = \eta^2(\{\boldsymbol{a}_b^i\}, \{\boldsymbol{a}_c^i\}) + w_b(\varphi_b^i)^2(\{\boldsymbol{a}_b^i\}) + w_c(\varphi_c^i)^2(\{\boldsymbol{a}_c^i\}) \tag{37}$$

where w_b^i and w_c^i are two weights attached to BCCs as discussed below.

Boundary regularization

The above formulation does not constrain the BC fields on boundaries (*i.e.,* a harmonic field may match any value on its boundary). An easy (and cheap) way to go around this issue is to assign the value of the average of their first neighbors to boundary nodes.

Regularization weights

The question of the weights given to regularization terms is always a difficult issue. Let us, however, point out that a characteristic length scale is hidden in the weights w_b and w_c. A dimensional analysis shows that each weight is proportional to the square of a length scale. Thus, if each cost function η^2, φ_b^2 and φ_c^2 in φ^2_{total} is normalized by its value computed for a trial field with a well-defined scale, then one can easily attach any scale to the regularization that then acts as a low-pass filter. Here, the chosen reference field is

$$v_{\text{ref}}(\mathbf{X}) = \exp\left(i\mathbf{n}\cdot\mathbf{X}/\xi\right) \tag{38}$$

where ξ is the characteristic length, and $\mathbf{n}$ an arbitrary unit vector. One can easily change the weight of Laplacian regularization w by setting a proper cut-off length ℓ

$$w = \left(\frac{\ell}{\xi}\right)^2 \frac{\eta^2(v_{\text{ref}})}{\varphi^2(v_{\text{ref}})} \tag{39}$$

To summarize, the Laplacian regularization dampens out high-frequency fluctuations of the corresponding field below a chosen length scale.

A.3 Temporal regularization

Previous work included a "soft" temporal regularization inside PGD-SC during the construction of temporal modes [18]. It consists in adding a low-pass filter to dampen out high-frequency temporal fluctuations. It is proposed to add a quadratic cost function to the L2-norm of the right-hand member $\mathbf{m}_{\text{W}}$

$$\chi^2(\mathbf{m}_{\text{W}}) = \int_{t_0}^{t_f} \left(\frac{\partial \mathbf{m}_{\text{W}}(\mathbf{X}, t)}{\partial t}\right)^2 \mathrm{d}t \tag{40}$$

Similarly, as for spatial regularization of BCCs, the weight of this additional cost function allows one to tune the cross-over time scale, τ, of this low-pass

filter. Using the discrete-time derivative in matrix form $[\mathbf{D}_t]$, regularized temporal modes are obtained from a generalized POD-like problem with a metric expressed as

$$\{\mathbf{m}_\mathrm{W}\}^\top \left([\mathbf{I}] + \tau^2 [\mathbf{D}_t]^\top [\mathbf{D}_t]\right) \{\mathbf{m}_W\} \tag{41}$$

Thus, after changing $\{\mathbf{m}_W\}$ into $\{\overline{\mathbf{m}}_W\} = \left([\mathbf{I}] + \tau^2 [\mathbf{D}]^\top [\mathbf{D}]\right)^{1/2} \{\mathbf{m}_\mathrm{W}\}$, the solution is still given by a mere POD of $\{\overline{\mathbf{m}}_W\}$ (additional details are given in Ref. [23]). This soft regularization allows the time scale τ to be adjusted at will with no side cost. Note that setting $\tau = 0$ enables the temporal regularization to be fully disabled.

References

[1] Field, J.E., Walley, S.M., Proud, W.G., Goldrein, H.T., Siviour, C.R.: Review of experimental techniques for high rate deformation and shock studies. International Journal of Impact Engineering **30**(7), 725–775 (2004). https://doi.org/10.1016/j.ijimpeng.2004.03.005. Fifth International Symposium on Impact Engineering

[2] Le Gourriérec, C., Chang, X., Durand, B., Roux, S.: High speed stereo-vision study of laminated glass fragmentation upon impact. Glass Structure and Engineering **8**, 423–442 (2023)

[3] Sutton, M.A., Orteu, J.J., Schreier, H.: Image Correlation for Shape, Motion and Deformation Measurements: Basic Concepts, Theory and Applications. Springer, New York, NY (USA) (2009)

[4] Hild, F., Roux, S.: Digital image correlation. In: Rastogi, P., Hack, E. (eds.) Optical Methods for Solid Mechanics. A Full-Field Approach, pp. 183–228. Wiley-VCH, Weinheim (Germany) (2012)

[5] Sutton, M.A.: Computer vision-based, noncontacting deformation measurements in mechanics: A generational transformation. Appl. Mech. Rev. **65**(AMR-13-1009), 050802 (2013)

[6] Dufour, J.-E., Hild, F., Roux, S.: Shape, Displacement and Mechanical Properties from Isogeometric Multiview Stereocorrelation. J. Strain Analysis **50**(7), 470–487 (2015)

[7] Passieux, J.-C., Bouclier, R., Périé, J.N.: A Space-Time PGD-DIC Algorithm:. Experimental Mechanics **58**(7), 1195–1206 (2018). https://doi.org/10.1007/s11340-018-0387-2

[8] Vu, H.-H., Labatut, P., Pons, J.-P., Keriven, R.: High accuracy and visibility-consistent dense multiview stereo. IEEE Transactions on Pattern Analysis and Machine Intelligence **34**(5), 889–901 (2012). https://doi.org/10.1109/TPAMI.2011.172

[9] Pagnacco, E., Caro-Bretelle, A.S., Ienny, P.: Parameter identification from mechanical field measurements using finite element model updating strategies. In: Grédiac, M., Hild, F. (eds.) Full-Field Measurements and Identification in Solid Mechanics, pp. 247–274. ISTE / Wiley, London (UK) (2012)

[10] Tong, W.: An evaluation of digital image correlation criteria for strain mapping applications. Strain **41**(4), 167–175 (2005) https://arxiv.org/abs/https://onlinelibrary.wiley.com/doi/pdf/10.1111/j.1475-1305.2005.00227.x. https://doi.org/10.1111/j.1475-1305.2005.00227.x

[11] Pan, B., Xie, H., Wang, Z.: Equivalence of digital image correlation criteria for pattern matching. Appl. Opt. **49**(28), 5501–5509 (2010). https://doi.org/10.1364/AO.49.005501

[12] Seitz, S.M., Curless, B., Diebel, J., Scharstein, D., Szeliski, R.: A comparison and evaluation of multi-view stereo reconstruction algorithms. In: 2006 IEEE Computer Society Conference on Computer Vision and Pattern Recognition (CVPR'06), vol. 1, pp. 519–528 (2006). https://doi.org/10.1109/CVPR.2006.19

[13] Dubreuil, L., Dufour, J.-E., Quinsat, Y., Hild, F.: Mesh-based shape measurements with stereocorrelation. Exp. Mech. **56**(7), 1231–1242 (2016)

[14] Pierré, J.-E., Passieux, J.-C., Périé, J.-N.: Finite Element Stereo Digital Image Correlation: Framework and Mechanical Regularization. Experimental Mechanics **57**(3), 443–456 (2017)

[15] Beaubier, B., Dufour, J.E., Hild, F., Roux, S., Lavernhe-Taillard, S., Lavernhe-Taillard, K.: CAD-based calibration of a 3D-DIC system: Principle and application on test and industrial parts. Exp. Mech. **54**(3), 329–341 (2014)

[16] Wang, Y., Charbal, A., Dufour, J.-E., Hild, F., Roux, S., Vincent, L.: Hybrid multiview correlation for measuring and monitoring thermomechanical fatigue test. Exp. Mech. **56**(DOI: 10.1007/s11340-019-00500-8), 845–860 (2019)

[17] Berny, M., Archer, T., Beauchêne, P., Mavel, A., Hild, F.: Displacement Uncertainty Quantifications in T3-Stereocorrelation. Experimental Mechanics **61**, 771–790 (2021)

[18] Chang, X., Le Gourriérec, C., Turpin, L., Berny, M., Hild, F., Roux, S.: Proper generalized decomposition stereocorrelation to measure kinematic fields for high speed impact on laminated glass. Computer Methods in Applied Mechanics and Engineering **415**, 116217 (2023). https://doi.org/10.1016/j.cma.2023.116217

[19] Chinesta, F., Ladeveze, P., Cueto, E.: A short review on model order reduction based on proper generalized decomposition. Archives of Computational Methods in Engineering **18**(4), 395 (2011). https://doi.org/10.1007/s11831-011-9064-7

[20] Charbal, A., Dufour, J.-E., Guery, A., Hild, F., Roux, S., Vincent, L., Poncelet, M.: Integrated Digital Image Correlation considering gray level and blur variations: Application to distortion measurements of IR camera. Optics and Lasers in Engineering **78**, 75–85 (2016). https://doi.org/10.1016/j.optlaseng.2015.09.011

[21] Charbal, A., Roux, S., Hild, F., Vincent, L.: Regularised digital-level corrections for infrared image correlation. Quantitative InfraRed Thermography Journal **15**(2), 172–193 (2018). https://doi.org/10.1080/17686733.2018.1425955

[22] Chang, X., Le Gourriérec, C., Hild, F., Roux, S.: Brightness and contrast corrections for stereocorrelation: Global and instantaneous formulation with spatial regularization. Mechanical Systems and Signal Processing **208**, 111057 (2024). https://doi.org/10.1016/j.ymssp.2023.111057

[23] Berny, M., Jailin, C., Bouterf, A., Hild, F., Roux, S.: Mode-enhanced space-time dic: applications to ultra-high-speed imaging. Measurement Science and Technology **29**(12), 125008 (2018)

[24] Martín, M., Centelles, X., Solé, A., Barreneche, C., Fernández, A.I., Cabeza, L.F.: Polymeric interlayer materials for laminated glass: A review. Construction and Building Materials **230**, 116897 (2020). https://doi.org/10.1016/j.conbuildmat.2019.116897

[25] Ahani, A., Ahani, E.: An overview for materials and design methods used for enhancement of laminated glass. Hybrid Advances **3**, 100063 (2023). https://doi.org/10.1016/j.hybadv.2023.100063

[26] European Norm: NF EN 356. Glass in building – Safety glazing – Testing and classification of resistance to manual attack (2000)

[27] Ball, A., McKenzie, H.: On the low velocity impact behaviour of glass plates. Le Journal de Physique IV **4**(C8), 8–783 (1994)

[28] Nourry, E.: Laminated glass behaviour under perforating impact. Thesis, Arts et Métiers ParisTech (March 2005). https://pastel.archives-ouvertes.fr/pastel-00001608

[29] Seshadri, M., Bennison, S.J., Jagota, A., Saigal, S.: Mechanical response of cracked laminated plates. Acta Materialia **50**(18), 4477–4490 (2002). https://doi.org/10.1016/S1359-6454(02)00255-0

[30] Del Linz, P., Hooper, P.A., Arora, H., Wang, Y., Smith, D., Blackman, B.R.K., Dear, J.P.: Delamination properties of laminated glass windows subject to blast loading. International Journal of Impact Engineering **105**, 39–53 (2017). https://doi.org/10.1016/j.ijimpeng.2016.05.015. Design and Analysis of Protective Structures 2015

[31] Elzière, P., Dalle-Ferrier, C., Barthel, E., Creton, C., Ciccotti, M.: Large strain viscoelastic dissipation during interfacial rupture in laminated glass. Soft Matter **13** (2017). https://doi.org/10.1039/C6SM02785G

[32] Bouzid, S., Nyoungue, A., Azari, Z., Bouaouadja, N., Pluvinage, G.: Fracture criterion for glass under impact loading. International Journal of Impact Engineering **25**(9), 831–845 (2001). https://doi.org/10.1016/S0734-743X(01)00023-9

[33] Leclerc, H., Neggers, J., Mathieu, F., Roux, S., Hild, F.: Correli 3.0. Agence pour la Protection des Programmes, Paris (France). IDDN.FR.001.520008.000.S.P.2015.000.31500 (2015)

[34] Jailin, C., Roux, S.: Modal decomposition from partial measurements. Comptes Rendus Mécanique **347**(11), 863–872 (2019). https://doi.org/10.1016/j.crme.2019.11.011. Data-Based Engineering Science and Technology

[35] Tikhonov, A.N., Arsenin, V.Y.: Solutions of Ill-posed Problems. J. Wiley, New York (USA) (1977)